A Herschel view of IC 1396 A

Sicilia-Aguilar, Aurora; Roccatagliata, Veronica; Getman, Konstantin; Henning, Thomas; Merín, Bruno; Eiroa, Carlos; Rivière-Marichalar, Pablo; Currie, Thayne

Published in:
Astronomy and astrophysics

DOI:
10.1051/0004-6361/201322609

Publication date:
2014

A&A 562, A131 (2014)
DOI: 10.1051/0004-6361/201322609

Astronomy & Astrophysics

A *Herschel* view of IC 1396 A: Unveiling the different sequences of star formation⋆

Aurora Sicilia-Aguilar[1,2], Veronica Roccatagliata[3], Konstantin Getman[4], Thomas Henning[5], Bruno Merín[6], Carlos Eiroa[1], Pablo Rivière-Marichalar[7], and Thayne Currie[8]

[1] Departamento de Física Teórica, Facultad de Ciencias, Universidad Autónoma de Madrid, 28049 Cantoblanco, Madrid, Spain
e-mail: aurora.sicilia@uam.es
[2] SUPA, School of Physics and Astronomy, University of St Andrews, North Haugh, St Andrews KY16 9SS, UK
[3] Universitäts-Sternwarte München, Ludwig-Maximilians-Universität, Scheinerstr. 1, 81679 München, Germany
[4] Department of Astronomy & Astrophysics, 525 Davey Laboratory, Pennsylvania State University, University Park PA 16802, USA
[5] Max-Planck-Institut für Astronomie, Königstuhl 17, 69117 Heidelberg, Germany
[6] Herschel Science Centre, ESAC-ESA. PO Box 78, 28691 Villanueva de la Cañada, Madrid, Spain
[7] Kapteyn Astronomical Institute, PO Box 800, 9700 AV Groningen, The Netherlands
[8] Department of Astronomy & Astrophysics, University of Toronto, Canada

Received 5 September 2013 / Accepted 11 December 2013

ABSTRACT

Context. The IC 1396 A globule, located to the west of the young cluster Tr 37, is known to host many very young stars and protostars, and is also assumed to be a site of triggered star formation.
Aims. Our aim is to test the triggering mechanisms and sequences leading to star formation in Tr 37 and similar regions.
Methods. We mapped IC 1396 A with *Herschel*/PACS at 70 and 160 μm. The maps reveal the structure of the most embedded parts of the star-forming site in great detail.
Results. The *Herschel*/PACS maps trace the very embedded protostellar objects and the structure of the cloud. PACS data reveal a previously unknown Class 0 object, labeled IC 1396 A-PACS-1, located behind the ionization front. IC 1396 A-PACS-1 is not detectable with *Spitzer*, but shows marginal X-ray emission. The data also allow the study of three of the Class I intermediate-mass objects within the cloud. We derived approximate cloud temperatures to study the effect and potential interactions between the protostars and the cloud. The Class 0 object is associated with the densest and coldest part of IC 1396 A. Heating in the cloud is dominated by the winds and radiation of the O6.5 star HD 206267 and, to a lesser extent, by the effects of the Herbig Ae star V 390 Cep. The surroundings of the Class I and Class II objects embedded in the cloud also appear warmer than the sourceless areas, although most of the low-mass objects cannot be individually extracted owing to distance and beam dilution.
Conclusions. The observations suggest that at least two episodes of star formation have occurred in IC 1396 A. One would have been the origin of the known, ~1 Myr-old Class I and II objects in the cloud, and a new wave of star formation would have produced the Class 0 source at the tip of the bright-rimmed cloud. From its location and properties, IC 1396 A-PACS-1 is consistent with having been triggered via radiative driven implosion (RDI) induced by HD 206267. The mechanisms behind the formation of the more evolved population of Class I/II/III objects in the cloud are uncertain. Heating of most of the remaining cloud by Class I/Class II objects and by HD 206267 itself may preclude further star formation in the region.

Key words. stars: formation – stars: protostars – stars: pre-main sequence – ISM: clouds – ISM: individual objects: IC 1396 A – open clusters and associations: individual: Trumpler 37/Tr37

1. Introduction

The IC 1396 A globule is part of one of the most remarkable H II regions in the northern hemisphere. Located on the western edge of the Tr 37 cluster (Marschall & van Altena 1987; Platais et al. 1998) at 870 pc distance (Contreras et al. 2002), it appears as a blown-away structure shaped by the stellar winds of the massive stars in Tr 37. The Trapezium-like system HD 206267, which is dominated by a O6.5 star (Abt 1986; Peter et al. 2012), is thought to be the main source of the ionization of IC 1396 A, which is located at about 4.5 pc projected distance to the west of HD 206267.

Tr 37 is part of the Cep OB2 region (Simonson & van Someren Greve 1976), which is considered as an example of triggered or sequential star formation (Elmegreen 1998). Loren et al. (1975) found strong molecular line emission associated with IC 1396 A, suggestive of material with different column densities and temperatures, and postulated the existence of embedded sources that would contribute to the heating of the cloud. IC 1396 A is a bright-rimmed cloud (BRC; Sugitani et al. 1991; Sugitani & Ogura 1994) that is believed to be suffering dispersal and collapse because of triggered star formation induced by the massive and intermediate-mass stars in Tr 37. Sugitani et al. (1991) proposed a triggered population of young stellar objects (YSOs) with IR excesses identified with IRAS. The star-formation sequence would have started with the 12 Myr old cluster NGC 7160, giving rise later on to the younger (4 Myr) Tr 37 cluster and associated structures (Patel et al. 1995, 1998). The Patel et al. (1995) CO observations also revealed a column

⋆ Based on observations obtained with the *Herschel* Space Telescope within open time proposal "Disk dispersal in Cep OB2", OT1_asicilia_1. *Herschel* is an ESA space observatory with science instruments provided by European-led PI consortia and with important participation from NASA.

density enhancement shaped by the ionization front of the BRC. The CO and NH_3 studies of Morgan et al. (2009, 2010) are also consistent with ongoing, probably triggered star formation as the origin of the Class I object at the edge of the southern part of IC 1396 A (21360798+572637/γ; Sicilia-Aguilar et al. 2006a,b; Reach et al. 2004). Nevertheless, conclusive evidence of triggered star formation based on gas kinematics is not always easy to obtain (e.g., Chen & Huang 2010; Mookerjea et al. 2012), since dynamical evolution may contribute to erasing the signatures of triggered star formation with time.

The *Spitzer* Space Telescope revealed a rich, embedded population of low-mass stars and protostars within IC 1396 A in great detail. *Spitzer* unveiled about 60 very embedded sources, mostly Class I/II, plus a similar number of low-mass and solar-type Class II/III objects located within <4′ (1 pc at 870 pc distance) of the globule (Reach et al. 2004; Sicilia-Aguilar et al. 2006a, 2013b; Morales-Calderón et al. 2009). *Chandra* X-ray observations revealed 250 objects in and near the BRC, doubling the previously known population down to masses ∼0.1 $M_\odot$ (Getman et al. 2012).

The stellar population associated with IC 1396 A is clearly differentiated in isochronal age. Not only do the objects in-cloud appear to be younger, but there is also evidence for a spatial age gradient: younger stars (≤1 Myr, according to the Siess et al. 2000 isochrones) appear in an arc-shaped region around IC 1396 A (Sicilia-Aguilar et al. 2005). X-ray detected sources also show isochronal age differences, with objects near the globule being as young as 1−2 Myr, while the main cluster population has typical ages of 4 Myr (Getman et al. 2012). There is also a spatial evolutionary-state gradient. While optical and *Spitzer* studies of the main Tr 37 cluster revealed only Class II and Class III sources, with a disk fraction about 48 ± 5% and disk IR excesses lower than Taurus (Sicilia-Aguilar et al. 2006a, 2013b), IC 1396 A contains Class II objects with Taurus-like disks and several embedded Class I sources (Reach et al. 2004; Sicilia-Aguilar et al. 2006a; Morales-Calderón et al. 2009).

The age gradient observed from the ionizing star HD 206267 towards the cloud suggests star formation due to radiative driven implosion (RDI) that could have lasted for several Myr. In the RDI scenario, the ionization front from OB stars ablates the surface of surrounding cloudlets, producing cometary structures and driving a compression shock inward, inducing star formation. Discussed since the 1980s, RDI has now well-developed hydrodynamical calculations and predictions (Kessel-Deynet & Burkert 2003; Miao et al. 2008). RDI could be responsible for a substantial part (∼14−25%) of the star formation in the region (Getman et al. 2012). Narrow-line imaging also reveals signs of ionization on the cloud's edge (Sicilia-Aguilar et al. 2004, 2013b; Barentsen et al. 2011), showing not only that HD 206267 has an effect on the cloud, but the low-mass T Tauri stars in the region also appear to interact with their surroundings, contributing to the removal and dispersal of the cloud material (Sicilia-Aguilar et al. 2013b). The most remarkable example may be the cleared, eye-like hole in the center of the globule, created by the intermediate-mass star V 390 Cep and the classical T Tauri star 14-141 (see Fig. 1).

Here we present the *Herschel*/PACS observations of IC1396 A. PACS scan maps at 70 and 160 μm were obtained as part of the open time program "Disk dispersal in Cep OB2" (PI A. Sicilia-Aguilar). In the present work we concentrate on the star formation and cloud structure of IC 1396 A. More detailed discussion of the stars with disks in the Cep OB2 region, including IC 1396 A and surroundings, will follow in a coming publication. The observations and data reduction are described in Sect. 2. Section 3 presents the analysis of the point sources and cloud structure. The discussion of the implications for the star formation history in the region are presented in Sect. 4, and Sect. 5 summarizes our results.

2. Observations and data reduction

The IC 1396 A globule was observed with the ESA *Herschel* Space Observatory (Pilbratt et al. 2010) using the Photodetector Array Camera and Spectrometer (PACS; Poglitsch et al. 2010). The observations comprised a large scan map (AORs 1342259791 and 1342259792) and a small minimap field (AORs 1342261853 and 1342261854). They were executed by *Herschel* on 2013 January 16 and 2013 January 23, respectively. The two AORs of the large map correspond to scan and cross-scan (at 45 and 135 degrees with respect to the array) of a 13.5′ × 13.5′ field centered on $21^h38^m18.770^s$ $+57^d31^m36.80^s$ at 70 and 160 μm. The minimap field was observed at the same wavelengths, centered on $21^h36^m25.080^s$ $+57^d27^m50.30^s$, and consisted of a scan and cross-scan at 70 and 110 degrees with respect to the array. The field was selected to contain the main part of the IC 1396 A globule, together with the younger disk population in Tr 37. The disk population of Tr 37 will be discussed in a separate paper. The large scan map was executed in 1.8 h, the small minimap required 20 min of *Herschel* time, and both used the medium (20″/s) scan speed. The final sensitivity of the image depends strongly on the presence of extended structures, resulting in a lower contrast in the areas dominated by the IC 1396 A globule emission than in the clean areas where the older, Class II/III Tr 37 population is located.

The data were reduced using HIPE[1] environment, version 11.0 (Ott et al. 2010) and the Unimap[2] software (Piazzo et al. 2012). The PACS data calibration is that of 2013 February 14. The basic corrections (up to level 1) were done with HIPE. The HIPE reduction was based on the standard Bright Source HIPE templates up to level 1. It included identifying the science frames, flagging the bad and saturated pixels, converting from ADUs to Volts, converting chopper angles to sky angles, computing the frame coordinates, and calibrating the data. The main complication of the region is the failure of the standard HIPE high-pass filtering (HPF) in a field where the extended emission is the main science target, so the final mapping was done with Unimap. First, the Unihipe interface was used with HIPE to produce the Unimap input files, which for PACS data are essentially the level 1 products.

Unimap is based on the generalized least square (GLS) mapping technique, but has additional features to remove offsets, cosmic rays, calibration and baseline drifts, and glitches (Piazzo et al. 2012). To take care of the distortion and noise resulting from the GLS processing, Unimap includes two post-GLS routines for removal of distortion and minimization of the map noise. After creating a naive map (containing signal and correlated noise) based on the level 1 HIPE results, Unimap searches for and flags signal jumps. Later on, it detects, flags, and corrects glitches by applying an HPF of 25″. Drifts are corrected by a subspace least square (SLS) technique. Noise corrections are applied by estimating the noise power and spectrum. Then the GLS map routine is applied, and if the distortion is stronger than the correlated noise, the map is further corrected, estimating the distortion by a median filtering and naive projection. This cor-

[1] HIPE is a joint development by the *Herschel* Science Ground Segment Consortium, consisting of ESA, the NASA *Herschel* Science Center, and the HIFI, PACS, and SPIRE consortia.

[2] See http://w3.uniroma1.it/unimap/ for further details.

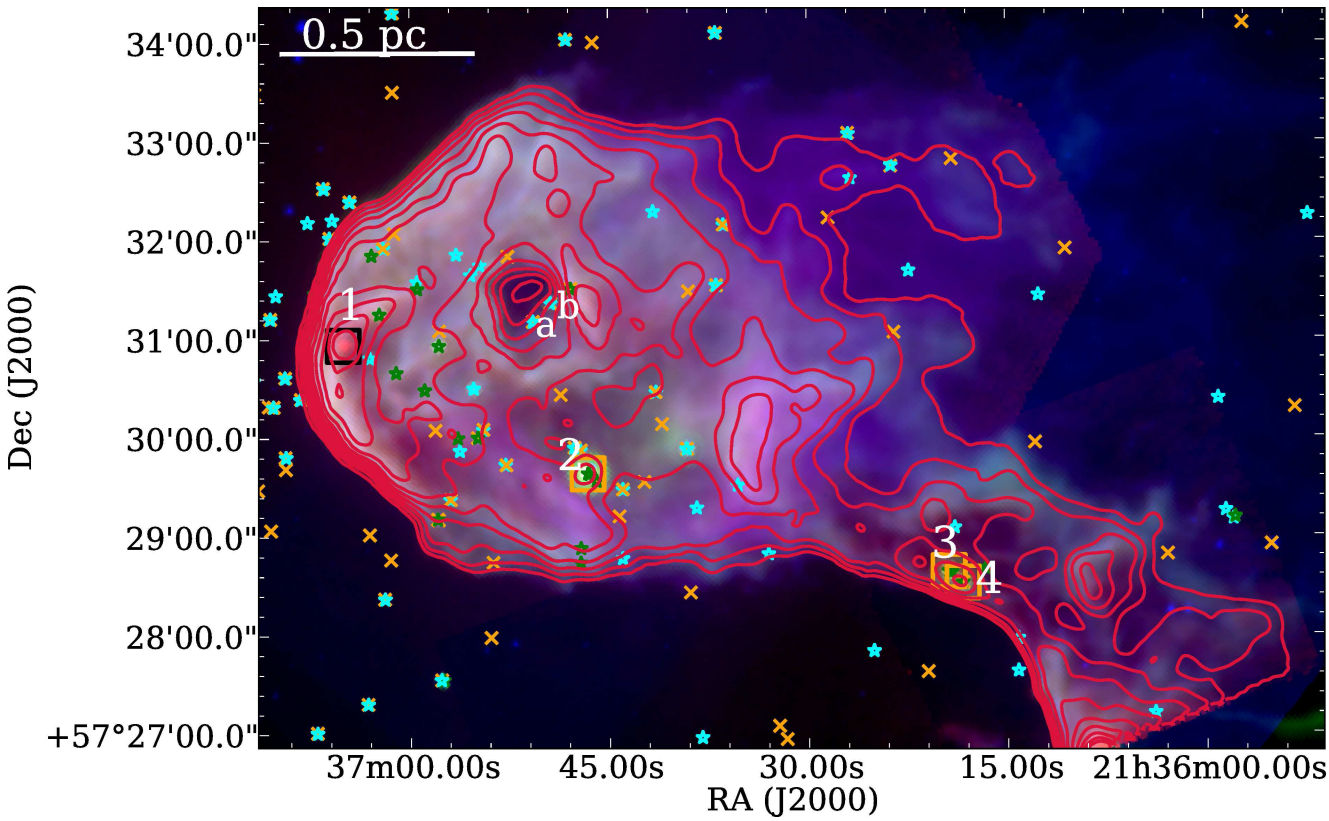

Fig. 1. A 3-color (8, 24, 70 μm) image of the IC 1396 A globule. The cyan stars denote Class II and Class III objects from Sicilia-Aguilar et al. (2005, 2006a,b), Morales-Calderón et al. (2009), and Getman et al. (2012). The green stars are Class I objects from Sicilia-Aguilar et al. (2006a) and Reach et al. (2004). The yellow X symbols correspond to X-ray detections consistent with YSO from Getman et al. (2012). The objects discussed in this work are marked as large squares (black for Class 0 objects, orange for Class I objects) and labeled with numbers (1 = IC 1396 A-PACS-1; 2 = 21364660+5729384; 3 = 21361942+5728385; 4 = 21361836+5728316). We also labeled the objects in the eye-shaped hole of the nebula (marked as cyan stars; a = V 390 Cep; b = 14-141, see text). The contours correspond to the 160 μm PACS image, 10 levels in log scale between 0.7 and 10 Jy/beam.

rection tends to increase the noise of the image, which is finally reduced by applying a weighted noise correction. The final map is projected with pixel sizes 2″ for the 70 μm image, and 3″ for the 160 μm image.

At present, Unimap does not allow large scan maps and minimaps to be combined. For photometry purposes, we used the individual maps, which involve less post-processing. To study the whole cloud structure, a combined, mosaicked map of the four AORs was constructed using the new mosaicking tool within HIPE version 11.0. We first used HIPE on the minimap to rotate it, trim its edges (to avoid an increase in the noise at the map edges affected by low coverage), and derotate it. We finally combined the rotated minimap and the larger scan map with the mosaicking tool. Because of the different orientations of the images, the final mosaic is resampled by HIPE to one third of the original pixel size. The final mosaicked maps around the IC 1396 A region are displayed in Fig. 1 (for a 3-color map including *Spitzer* data) and Fig. 2 (for a detailed view of the *Herschel*/PACS data at both wavelengths).

3. Analysis

3.1. Source photometry and luminosities

Given the strong extended emission throughout the area and the beam dilution for a region located at 870 pc, only four point sources are clearly identified in the region (see Table 1 and Fig. 2). Three of them correspond to the known intermediate-mass Class I candidates 21361836+5728316, 21361942+5728385, and 21364660+5729384 (Sicilia-Aguilar et al. 2006a), also known as δ, ϵ, and α from Reach et al. (2004). The IRAS source 21346+5714 (Sugitani et al. 1991), corresponding to source γ or 21360798+572637 (Reach et al. 2004; Sicilia-Aguilar et al. 2006a), is marginally detected on the edge of the image. It appears brighter, redder, and more extended than 21364660+5729384, since it is probably a more massive, less evolved object, but since it is cut at the edge of the image, we cannot extract any photometric information. The fourth object is a new source located at 21:37:05.04 +57:30:56.4 (Fig. 3), which we name IC 1396 A-PACS-1. This new source is significantly brighter and more extended at 160 μm than at 70 μm (see Table 1). The compact part of the source is surrounded by an arc-like extended emission that shows a remarkable flux gradient following the contours of the ionized front of the BRC. IC 1396 A-PACS-1 and its associated arc-like emission clearly dominate the IC 1396 A map at 160 μm. This source was not detected with *Spitzer*, and the only previous detection of a source at the same position corresponds to a X-ray source not labeled as a cluster member owing to its low significance (Getman et al. 2012; X-ray source # 248, with only 3 X-ray net counts).

To quantify the fluxes of the sources, we performed aperture photometry with IRAF[3]. We selected 6″ and 9″ apertures for the 70 and 160 μm images and their corresponding aperture

[3] IRAF is distributed by the National Optical Astronomy Observatories, which are operated by the Association of Universities for Research in Astronomy, Inc., under cooperative agreement with the National Science Foundation.

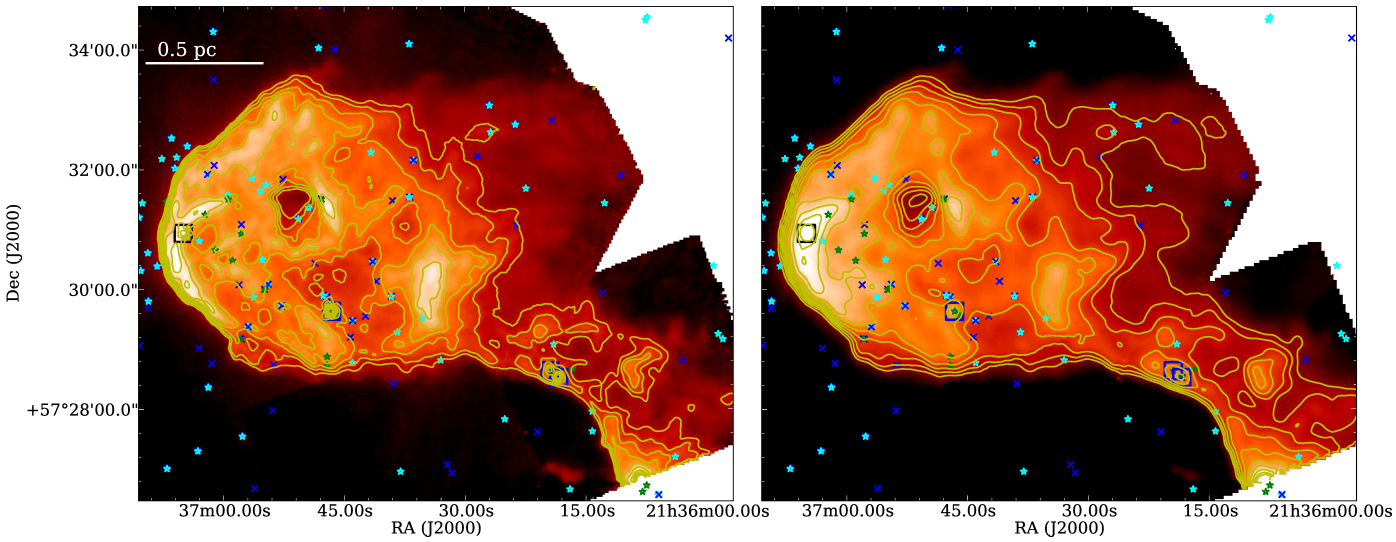

Fig. 2. IC 1396 A as seen at 70 (*left*) and 160 μm (*right*). The cyan stars denote Class II and Class III objects from Sicilia-Aguilar et al. (2005, 2006a,b), Morales-Calderón et al. (2009), and Getman et al. (2012). The green stars are Class I objects from Sicilia-Aguilar et al. (2006a) and Reach et al. (2004). The blue X symbols correspond to X-ray detections consistent with YSO from Getman et al. (2012). The objects discussed in this work are marked as large squares (black for Class 0 objects, blue for Class I objects). The contours mark 10 levels in log scale from 0.1−2.0 Jy/beam (70 μm) and 0.7−10 Jy/beam (160 μm).

Table 1. Source photometry and integrated luminosities.

Source name	RA (J2000)	Dec (J2000)	$F_{70\ \mu m}$ (Jy)	$F_{160\ \mu m}$ (Jy)	$L_{integrated}$ ($L_\odot$)	Class	Other IDs[c]
IC 1396 A-PACS-1	21:37:05.04	+57:30:56.4	2.32 ± 0.23	25.5 ± 2.6	1.5 ± 0.1	0	
21364660+5729384	21:36:46.60	+57:29:38.4	3.31 ± 0.33	3.2 ± 0.3	1.00 ± 0.08	I	α
21361942+5728385	21:36:19.42	+57:28:38.5	0.97 ± 0.10	5.4 ± 1.1[a]	0.22 ± 0.10[b]	I	ϵ
21361836+5728316	21:36:18.36	+57:28:31.6	1.49 ± 0.15	5.4 ± 1.1[a]	0.26 ± 0.10[b]	I	δ

Notes. Photometry of the known cluster members detected by *Herschel*/PACS in IC 1396 A, and their integrated luminosities (taking the ancillary data for the Class I sources into account, see Table 2). The 160 μm flux for 21361836+5728316 and 21361942+5728385 corresponds to both sources, which appear merged in the image, with the peak flux close to the position of 21361836+5728316. [(a)] The flux includes both sources, which are merged at 160 μm. [(b)] Luminosities for these sources are very uncertain due to the lack of observations at longer and shorter wavelengths, and the fact that the 160 μm data point includes both objects. [(c)] Alternative IDs from Reach et al. (2004).

corrections of 1.597 and 1.745, according to the PACS manual. To avoid potential uncertainties induced by resampling in the final map, the photometry was done in the individual fields (large map and minimap). Considering the spatially variable cloud emission in IC 1396 A, we estimated the sky emission for the photometry by measuring different locations around the sources. The errors were derived considering the average sky rms and the correlated noise due to oversampling estimated as $(3.2/\text{pixsize})^{0.68}/0.95$ and $(6.4/\text{pixsize})^{0.73}/0.88$ for 70 and 160 μm, respectively (Mora priv. comm.). Here, pixsize is the selected pixel size in the projected maps (2″ for the 70 μm map and 3″ for the 160 μm map), although after including further calibration errors and the uncertainties due to strong, highly variable nebular emission, we obtain nominal errors of 10%. All Class I sources appear point-like at both wavelengths, but IC 1396 A-PACS-1 is clearly extended at 160 μm and may be marginally resolved at 70 μm (see Sect. 3.2). Therefore, its 160 μm flux is likely a lower limit, although treating it as point-like at 70 μm should be accurate. The photometry of the individual sources is listed in Table 1.

We estimated the total luminosity of the objects by integrating their SEDs. Except for the new source IC 1396 A-PACS-1, the other three objects had been observed in the near- and mid-IR by 2MASS and/or *Spitzer* (Table 2), so we simply integrated their SEDs as traced by the literature data and the *Herschel*/PACS observations, and extrapolating to modified black body emission out of the observed wavelength ranges. For 21361836+5728316 and 21361942+5728385, the lack of near-IR detections and the uncertain 160 μm flux (due to source merging and cloud emission) result in a high uncertainty, although both sources are clearly less luminous than 21364660+5729384. For 21364660+5729384 we have a more complete dataset and are able to detect the turndown of the SED at high and low frequency, so the estimate is more accurate.

For IC 1396 A-PACS-1, we follow the procedure in Sicilia-Aguilar et al. (2013a), based on Ward-Thompson et al. (2002). We assume that the emission of the Class 0 source can be reproduced by a modified black body, given by

$$F_\nu = B_\nu(T)(1 - e^{-\tau_\nu})\Omega. \quad (1)$$

Here, F_ν is the flux density, B_ν(T) the black body emission for a temperature T, τ_ν the frequency-dependent optical depth, and Ω the solid angle subtended by the source. Considering that at long wavelengths, the optical depth follows a power law with frequency, $\tau_\nu \propto \nu^\beta$, it is possible to estimate the source temperature, although for IC 1396 A-PACS-1 the uncertainty is large because we only have two photometric points. Taking the values from Ward-Thompson et al. (2002) for $\beta = 2$ and $\tau_{200\ \mu m} = 0.06$, we obtain a good fit for a temperature of 17 K, consistent with a prestellar core or Class 0 object (see Fig. 4). A flatter frequency

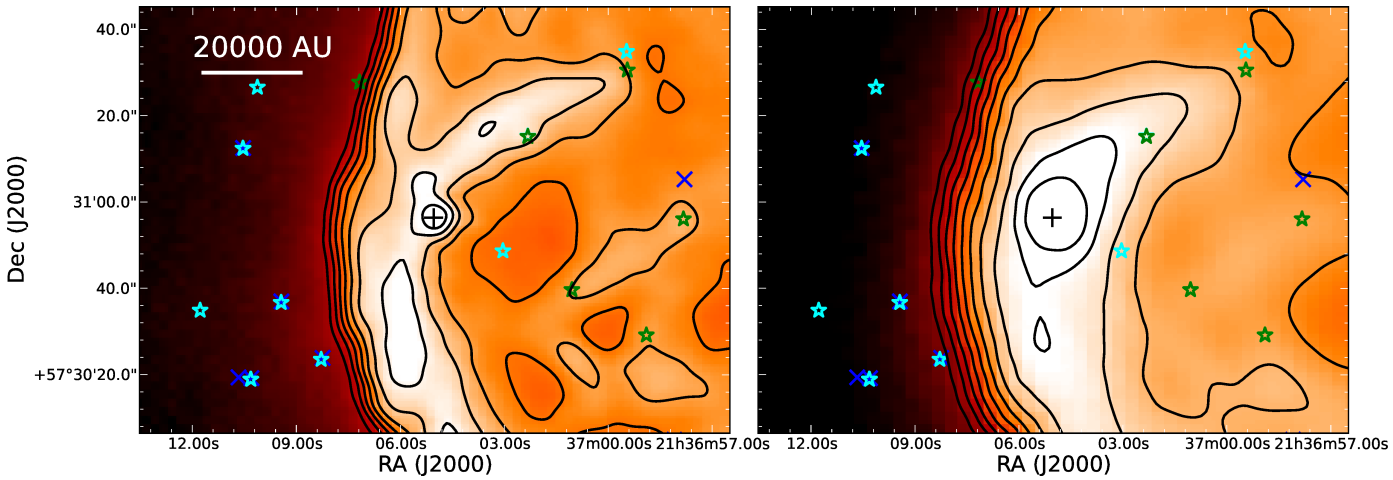

Fig. 3. Zoom in the surroundings of the newly discovered source IC 1396 A-PACS-1 at 70 μm (*left*) and 160 μm (*right*). The black + marks the center of the new source, according to the 70 μm map. The cyan stars denote Class II and Class III objects from Sicilia-Aguilar et al. (2005, 2006a,b), Morales-Calderón et al. (2009), and Getman et al. (2012). The green stars are Class I objects from Sicilia-Aguilar et al. (2006a) and Reach et al. (2004). The blue X symbols correspond to X-ray detections consistent with YSO from Getman et al. (2012). The contours mark 10 levels in log scale from 0.1−2.0 Jy/beam (70 μm) and 0.7−10 Jy/beam (160 μm).

Table 2. Ancillary data for the Class I sources.

	21361836 +5728316	21361942 +5728385	21364660 +5729384
Filter	Flux (Jy)	Flux (Jy)	Flux (Jy)
J	–	–	<4E-4
H	–	–	9E-4 ± 1E-4
K	–	–	5.4E-3 ± 1E-4
3.6 μm	3.2E-3 ± 4E-4	2.9E-3 ± 3E-4	4.3E-2 ± 4E-3
4.5 μm	1.03E-2 ± 6E-4	8.2E-3 ± 6E-4	7.6E-2 ± 8E-3
5.8 μm	2.6E-2 ± 1E-3	1.76E-2 ± 9E-4	0.21 ± 0.02
8.0 μm	3.3E-2 ± 2E-3	2.6E-2 ± 1E-3	0.20 ± 0.02
24 μm	0.346 ± 4E-3	0.355 ± 0.004	1.56 ± 0.16

Notes. 2MASS and *Spitzer* IRAC/MIPS data for the Class I sources detected with *Herschel*/PACS. 2MASS data from Cutri et al. (2003). *Spitzer* data from Sicilia-Aguilar et al. (2006a).

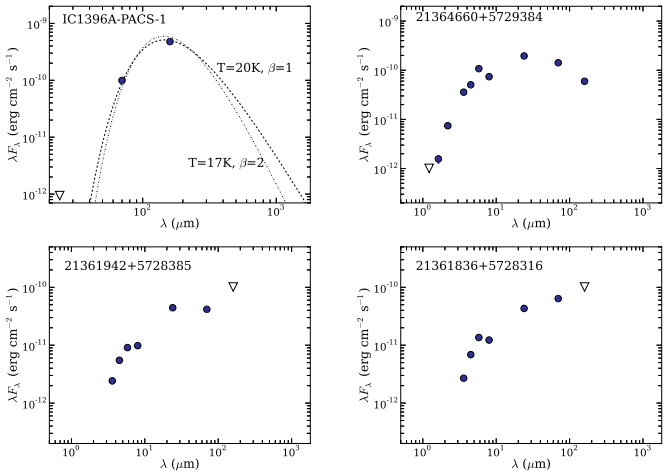

Fig. 4. SEDs of the four sources detected in the IC 1396 A globule. For IC 1396 A-PACS-1 we also display comparative modified black body models with different temperatures and frequency power laws (see text). Filled circles correspond to detections (error bars are generally smaller than the points), open inverted triangles are upper limits.

dependence $\beta = 1$ (that could be related to grain growth) produces a slightly better fit for a temperature of 20 K, still consistent with the hypothesis of a Class 0 object. The solid angle subtended by the object (Ω) is also fitted in this simple model. Models with lower T predict larger object radii. In this case, the model with $T = 17$ K, $\beta = 2$ would result in an object larger than the compact source at 70 μm (~9.7″), while the model with $T = 20$ K, $\beta = 1$ is more consistent with a compact source (radius ~6.8″), even though both models are too simple to offer strong constraints on the object size.

3.2. Source classification

Source 21364660+5729384 is brighter at 70 μm than at 160 μm. Sources 21361836+5728316 and 21361942+5728385 are merged and surrounded by bright structures at 160 μm that make their fluxes very uncertain. Both sources are probably brighter at 160 μm, especially 21361942+5728385. The 160 μm extended detection peaks at the position of this source. They are thus probably in a more embedded/earlier evolutionary phase than 21364660+5729384. Despite the uncertainties caused by merging, sources 21361836+5728316 and 21361942+5728385 are clearly less luminous than 21364660+5729384 at the observed wavelengths. We traced the SEDs of all objects (Fig. 4) including all previous data available in the literature (Table 2), which are consistent with Class I sources, as previously suggested by *Spitzer* (Reach et al. 2004; Sicilia-Aguilar et al. 2006a,b). The SEDs of these three sources show the characteristic low 8 μm emission compared to the rest of bands, suggestive of a silicate absorption feature, typical of Class I sources.

The SED and far-IR brightness of IC1396A-PACS-1 and the fact that it does not present any emission at 24 μm suggest that it corresponds to a Class 0 or transition Class 0/I object, the only one known within IC 1396 A. Given the complexity of the cloud emission, we computed the MIPS 24 μm flux upper limit based on both the faintest sources detectable on similar backgrounds, and the sky rms in the position of the object, obtaining for both cases a very similar result of 3σ upper limit 7.5 mJy at 24 μm (see Fig. 4). This sets a very strong constraint on the total flux emission of the object at shorter wavelengths. Its relatively high luminosity compared to the rest of embedded cloud members

suggest it could be the progenitor of an intermediate-mass star, although with our resolution we cannot exclude the presence of a small group of objects.

IC 1396 A-PACS-1 is clearly extended at 160 μm, which would be compatible with it being a starless core or a Class 0 object, but the 70 μm image reveals a compact source (Fig. 3). Determining whether the compact source is point-like is more complicated. Its size is comparable to that of the PACS PSF ($FWHM$ = 5.6″, beam diameter 6.7″), but the three-lobe structure of the PACS point spread function (PSF), which is clearly visible for the three Class I sources and other point-like objects in the field, is not clear for IC 1396 A-PACS-1. This could indicate that the object is marginally resolved by PACS, although it could also be the result of the strong background emission around the source. Taking this into account, for a distance of 870 pc, we estimate that the compact source has a size of ≤6000 AU. At 160 μm, the source is extended, with an elliptical core slightly more elongated than the PSF (>11.4″, ∼10^4 AU at 870 pc) that merges without clear boundaries into the extended arc-like rim. At 160 μm we would thus mostly observe the envelope emission, with a typical size close to ∼0.1 pc, but strongly elongated following the cloud contours that are shaped by the ionization front coming from HD 206267. The estimated size at 160 μm is consistent with the expectations for Class 0 objects (e.g., Lippok et al. 2013), even though it is hard to define the source boundaries at this wavelength and the whole structure is strongly asymmetric. More dynamical information would be needed to determine the extent of the envelope that will collapse onto the central source(s), since part of the structure may be simply related to the surrounding cloud.

From the compact size and the lack of significant energy output at wavelengths ≤24 μm, we conclude that the source is most likely a Class 0 object. On the other hand, the marginal (<3σ) X-ray emission found by Getman et al. (2012) precisely at the location of the new source is intriguing. If the detected weak X-ray emission were associated to the source itself, it could point to a later evolutionary stage than Class 0 (e.g., in transition between the Class 0 and Class I stages), since X-ray emission from Class 0 objects is rare and/or very weak (Preibisch 2004; Prisinzano et al. 2008; Giardino et al. 2006), even though the emission would still be much weaker than observed towards typical IC 1396 A Class I sources. But if the X-ray emission is associated to jets in the region (Pravdo et al. 2001; Favata et al. 2002; Sicilia-Aguilar et al. 2008), we cannot use it as a constraint on the source class.

3.3. Temperature and cloud structure from Herschel observations

Following a similar scheme to the one in Sicilia-Aguilar et al. (2013a), we studied the temperature structure of the cloud. We resampled both images at 70 μm and 160 μm to the same 3″/pixel scale, created a new mosaic with the HIPE mosaicking tool (resulting in a resampling of 1″/pixel scale), and derived a ratioed image by dividing the blue by the red one. The temperature per pixel is then derived based on a modified black body scheme (Preibisch et al. 2013; Roccatagliata et al. 2013). This method is well suited to tracing the warmer cloud surface temperature. On the other hand, SED fitting (using PACS and SPIRE data; Roccatagliata et al. 2013) computes the beam-averaged dust temperature along the line-of-sight and is more sensitive to the densest (and thus coolest) central parts of clouds. Roccatagliata et al. (2013) find that the temperatures derived from ratioed maps are typically ∼5% higher than the temperatures derived from the SED fitting. This result is expected because the color temperature is biased toward the warmer cloud surface. In addition, there is a known degeneracy between the dust color temperature and spectral index (Juvela et al. 2013), which produces different biases depending on the method used to derive T and β from submillimeter observations. In our case, since we only have observations at 70 and 160 μm, our result is approximate.

To construct our temperature maps, we consider that the emission from each pixel is due to a modified black body (similar to Eq. (1)) for a single temperature. Considering the same solid angle Ω at both wavelengths, the ratio of fluxes at 70 and 160 μm can be thus written as:

$$\frac{F_{\nu,70}}{F_{\nu,160}} = \frac{B_{\nu,70}(T)(1-\mathrm{e}^{-\tau_{\nu,70}})}{B_{\nu,160}(T)(1-\mathrm{e}^{-\tau_{\nu,160}})}. \quad (2)$$

If we take $\beta = 2$, the flux ratio between two wavelengths is thus a function of T alone. This way, we can trace the temperature structure pixel-by-pixel for the entire cloud (Fig. 5). For this exercise, we excluded the pixels with fluxes below 0.0014 Jy/pix (at 70 μm) and below 0.0015 Jy/pix (at 160 μm; for the HIPE-resampled pixel size 1″) to avoid uncertainties caused by the typical image noise. Therefore, the only significant values of the temperature are those inside the globule. The surroundings of the IC 1396 A, corresponding to the H II region around the cluster Tr 37, have uncertain fluxes due to the nearby bright globule and to the low background, which can lead to some unphysical temperature distributions out of the BRC.

A comparison of the temperature structure with the location of the known Class I/II/III sources reveals that the sources are on slightly warmer (T > 21 K), net-like structures throughout the cloud. Part of this may be the effect of beam dilution on faint, distant sources with far-IR emission. Since not all warm structures observed in the cloud have associated *Spitzer*/X-ray sources, there is also the possibility that embedded sources are also heating their surroundings, in a similar way to what we observe around V 390 Cep. The main difference would be the lower mass (and energetic output) of most of the Class I/II/III sources in the globule. Warmer, sourceless areas may be associated with external heating by HD 206267. Cloud heating by low-mass sources is also seen in low-mass regions like the Coronet cluster (Sicilia-Aguilar et al. 2013a).

IC 1396 A-PACS-1 is surrounded by a cold area, but its central part is clearly hotter, revealing incipient star formation. A comparison of the temperature map with archival JCMT CO(3−2) data[4] shows that the CO emission is correlated with the known Class I/II/III sources and the warmest areas of the globule, while the area around IC 1396 A-PACS-1 does not have any significant CO emission above the plateau level observed in the coldest areas of the cloud. The archival data corresponds to CO(3−2) fluxes integrated over a 0.9 GHz window, so it not possible to obtain any significant dynamical information of the region or its objects. The lack of CO emission is consistent with the low temperatures in the area around IC 1396 A-PACS-1. Even though CO emission from outflows would be expected for a Class 0/I object, the lack of velocity resolution of the available JCMT data, together with the strong cloud emission, does not allow us to distinguish potential source-related emission. Starless cores are typically affected by CO depletion (Caselli et al. 1999; Bergin et al. 2002; Nielbock et al. 2012; Lippok et al. 2013), but

[4] http://www4.cadc-ccda.hia-iha.nrc-cnrc.gc.ca/data/pub/JCMT

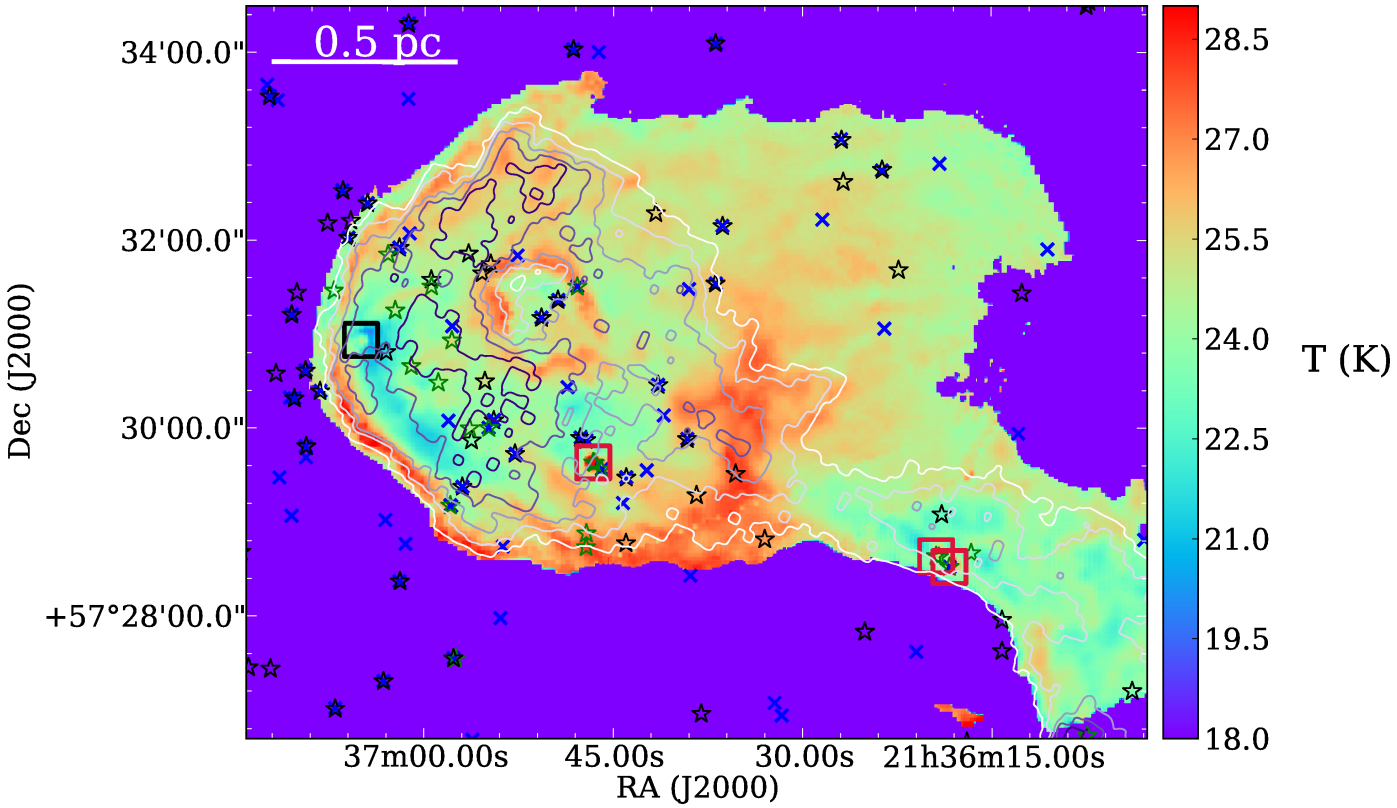

Fig. 5. Temperature map for IC 1396 A (see text). The contours mark the 10, 20, 30, 40, 50 K km s^{-1} levels of the integrated CO(3−2) emission from archival JCMT data. The black stars denote Class II and Class III objects from Sicilia-Aguilar et al. (2005, 2006a,b), Morales-Calderón et al. (2009), and Getman et al. (2012). The green stars are Class I objects from Sicilia-Aguilar et al. (2006a) and Reach et al. (2004). The blue X symbols correspond to X-ray detections consistent with YSO from Getman et al. (2012). The objects discussed in this work are marked as large squares (black for Class 0 objects, red for Class I objects). Note that due to the exclusion of pixels with low fluxes (see text), the only significant temperatures are those inside the globule and not those in the external parts that appear violet in the image.

IC 1396 A-PACS-1 is too compact and too bright to be considered starless. Further observations, especially velocity-resolved ones, would be needed to confirm whether the object presents distinct CO emission. In the case of a CO depleted object, considering the critical number density values for CO depletion ($n > 10^5$ cm^{-3}; Caselli et al. 1999) and a minimum size of the core as seen at 160 μm (~15″×20″, or ~13 000 AU × 17 400 AU as seen in projection), we would expect a mass of nearly 10 $M_\odot$ in the core. Although the object size is uncertain, and a distinct, compact object is resolved at 70 μm, these mass estimates agree with the object being the progenitor of an intermediate-mass star or a small stellar group (as observed, for instance, in highly fragmented clouds like the Coronet cluster; Sicilia-Aguilar et al. 2013a).

4. Discussion: sequential and triggered star formation in Tr 37

The cometary structure of the BRC IC 1396 A has been identified for a long time as a region shaped by the star HD 206267 (Loren et al. 1975) and as a potential site for triggered star formation (Sugitani et al. 1991; Patel et al. 1995; Reach et al. 2004; Sicilia-Aguilar et al. 2005, 2006a; Morgan et al. 2009, 2010; Getman et al. 2012). The new Class 0 object IC 1396 A-PACS-1 at the tip of IC 1396 A is a sign that the star formation process is not finished yet in the region. We do not find evidence of any further star formation, even though contrast problems with the cloud emission mean we cannot exclude the presence of further low-luminosity Class 0 objects. Nevertheless, the temperature map (Fig. 5) suggests that only the tip of the BRC behind the ionization rim has temperatures that are low enough to allow the formation of new stars, in agreement with archival CO JCMT observations.

IC 1396 A appears consistent with what one would expect from RDI-triggered star formation. The warmer outer dust layer can be a tracer of the ionization front (similar to Fig. 2 in Bisbas et al. 2011), and the cold, extended structure that harbors IC 1396 A-PACS-1 lies right behind the ionization front. This would agree with the general/qualitative RDI picture where dense cores form at the edges of the cloud between the ionization front and the compression shock. However, there is a substantial difference between the observations of IC 1396 A and the simulations of Bisbas et al. (2011) and others: they model small 5−10 $M_\odot$ cloudlets. These small cloudlets are expected to form a few low-mass stars within <1 Myr years before being completely ablated and photoevaporated. In contrast, IC 1396 A is a much larger globule, comparable to others such as IC 1396 N and Cep B (>200 $M_\odot$; Getman et al. 2007, 2009, 2012). In these larger regions, the triggered star formation does not appear restricted to a single short episode, but is instead a multi-episodic (or continuous) process that can last for many Myr years.

With the typical velocity dispersal observed in the low-mass members of Tr 37 (Sicilia-Aguilar et al. 2006b), stars are expected to move from their formation sites at a rate of about 1−2 pc per Myr. This is comparable to the size of the IC 1396 A globule for the age of Class I systems found within it. Nevertheless, the lack of Class I sources out of IC 1396 A and the presence of small, distinct miniclusters within Tr 37 suggest

that for ages about 1 Myr, dynamical evolution is not yet important in this region. These miniclusters consist of compact (<0.5 pc) groups of a few (2−10) stars with higher IR excesses and accretion rates than the main cluster. Sometimes they are also associated to small patches of nebulosity, all suggesting that they are younger than the surrounding, more evolved population (Barentsen et al. 2011; Getman et al. 2012; Sicilia-Aguilar et al. 2013b). These miniclusters could be a sign that star formation does not progress in a uniform way and several episodes of star formation may occur, even on scales as small as 0.5 pc, suggesting "clumpy" or multi-episodic star formation within the same cloud. The formation of IC 1396 A-PACS-1 at the tip of the cloud and surrounded by younger Class I/II objects may also explain the origin of the miniclusters. Getman et al. (2009) proposed two distinct scenarios for RDI star formation: slow shock propagation through the globule (where stellar kinematics and dynamical drift is important), and fast shock propagation (where stellar kinematics plays a less important role). The star formation efficiency in the Cep B cloud supported the second scenario, which also seems to be the case for IC 1396 A.

IC 1396 A-PACS-1 fits in this picture of continuous/multi-episodic triggered star formation. Given the age and evolutionary state differences between IC 1396 A-PACS-1 and the rest of the IC 1396 A population, other possibilities could be spontaneous star formation or triggering related to outflows from the previous population in the cloud. However, the position of the Class 0 source and the arc-shaped structure with a very steep gradient at far-IR wavelengths, as seen with *Herschel*/PACS, suggests some causal link between the ionization front and the object. Our [S II] imaging of IC 1396 A did not reveal any outflows in the surroundings of IC 1396 A-PACS-1, despite finding strong forbidden line emission at the ionization front, at the edge of the bubble created by V 390 Cep (especially near the low-mass star 14-141), and some weaker outflow emission probably associated with 21364660+5729384 or another of the lower mass Class I objects (Sicilia-Aguilar et al. 2013b). The *Herschel* data, together with our previous observations, thus favor the scenario where several distinct episodes of sequential or triggered star formation have occurred. The age and evolutionary stage gradient observed between the Tr 37 cluster and the Class I/II population associated with IC 1396 A (Sicilia-Aguilar et al. 2005, 2006a; Barentsen et al. 2011; Getman et al. 2012) shows that, after formation of the main Tr 37 cluster approximately 4 Myr ago, a second generation of stars was born to the west only ∼1−2 Myr ago, and star-building is still active in the cloud. The Class I/II objects are located in the less dense parts of the cloud, maybe because most of the original material is now dispersed or in the process of being dispersed, after suffering irradiation from HD 206267 and from the new generation of YSO.

Although most of the *Spitzer*-identified Class I/II objects within IC 1396 A cannot be individually resolved with PACS owing to their lower luminosity and the high cloud background, the *Herschel* observations suggest that these low-mass stars may be responsible for heating and dispersal of the cloud on small scales. These objects correspond mostly to solar-type and low-mass stars/protostars (below 2 $M_{\odot}$ and down to ∼0.1 $M_{\odot}$; Sicilia-Aguilar et al. 2005, 2013b; Getman et al. 2012) and appear spatially related to the warmest parts of the cloud (Fig. 5). HD 206267 could also be the heating source for the warm structure observed around 21:36:36, 57:30:30. In this case, we would expect this structure to be raised towards the observer, receiving full illumination by the O6.5 star. Only the denser part of the cloud, where the column density is higher and the temperature lower, would have started its collapse very recently, given rise to the Class 0 object IC 1396 A-PACS-1. If the cloud heating and dispersal continue as observed, this object may be the last one formed in the region, and may evolve into a structure similar to γ/21360798+572637 once the less dense parts of the cloud have been eroded. Nevertheless, considering that temperature maps are dominated by the higher temperatures in the region, our maps of the IC 1396 A region may be affected by the hotter, ionized cloud surface, which is directly exposed to the action of the massive and intermediate stars in Tr 37. More observations (e.g., high spatial-resolution line observations) would be required to exclude the presence of undetected cold and dense clumps that may continue to form stars in the region.

Even including the observed IR and X-ray sources, the stellar density of the cloud is much lower than found in sparse associations like the Coronet cluster (Sicilia-Aguilar et al. 2013a), even after correcting for completeness and distance differences. The Coronet cloud is substantially cooler than the IC 1396 A region because of the lack of external ionizing sources. The heating in the embedded parts of the Coronet appears to be exclusively related to the intermediate- and low-mass sources within the cloud. If star formation is halted by external cloud heating and dispersal, the initial conditions of Class I and Class II objects in and around IC 1396 A will be very different from those observed in the sparse associations, which could also affect the subsequent disk evolution.

The effect of a large number of OB stars on the remnant cloudlets in more massive star-forming regions will be more dramatic than in IC 1396 A. For instance, the Carina Nebula Complex extends over more than 80 pc in the sky, and it contains at least 65 O-type stars and four Wolf-Rayet stars. The average temperature of most of the complex is about 30 K, while at the edge of the nebula, the clouds temperature decrease down to 26 K (Roccatagliata et al. 2013). The hotter parts of the cloud are located in the central region around η Car (∼25 pc × 25 pc), which hosts the young clusters Trumpler 14, 15, and 16 and contains about 80% of the high-mass stars of the entire complex. The temperatures are between 30 and 50 K (excluding the position of η Car itself, which reaches values of 60 K). The local temperature of the cloud is related to the number of high-mass stars in the cluster. In such environments, the potential for several sequences of star formation would be expected to be more limited, due to the extreme disruption of cloudlets and the higher temperatures of the surrounding environment.

5. Summary

We present the first results of our open time *Herschel* proposal on the Tr 37 cluster. We used PACS observations at 70 and 160 μm to trace the BRC IC 1396 A, previously known to host a population of T Tauri and Class I objects with ages younger than the main Tr 37 cluster. Our results can be summarized as follows:

- We identified for the first time a Class 0 object within the IC 1396 A globule, labeled as IC 1396 A-PACS-1. It is the only Class 0 candidate known in the region. This object was not detected with *Spitzer*, although there is a low-significance X-ray detection that could be related to it. The object is located in the coldest, CO-depleted region of the cloud, directly behind the ionized rim. Its estimated luminosity (∼1.5 ± 0.1 $L_{\odot}$) suggests that it is the precursor of an intermediate-mass star or a small stellar group.
- Three of the Class I sources in IC 1396 A were also detected with *Herschel*/PACS, completing their *Spitzer* and 2MASS data and confirming their classification. Their

luminosities suggest that they are precursors of solar-mass to intermediate-mass stars.

- The discovery of the new Class 0 object IC 1396 A-PACS-1 suggest multi-episodic star formation in the region. Previous episode(s) would have given birth to the embedded Class I and Class II objects in IC 1396 A, while a later one would have produced IC 1396 A-PACS-1 in the densest and coldest part of the cloud. The position of IC 1396 A-PACS-1 with respect to the ionization front observed in the BRC is consistent with triggered star formation via RDI.
- The presence of two populations with different ages, resulting from distinct star formation episodes within the IC 1396 A cloud, may also explain the miniclusters observed in Tr 37. These miniclusters consist of small groups of stars, sometimes surrounded by nebulosity, that appear younger than the main Tr 37 population. Miniclusters could result from clumpy or multi-episodic star formation within the same cloud, as observed in IC 1396 A.
- The temperature map of IC 1396 A shows that heating in the cloud responds to two mechanisms: strong external heating by the O6.5 system HD 206267 and, to a lesser extent in the most embedded parts, localized heating by stars and protostars within the cloud. The most massive stars (e.g., V 390 Cep) also contribute to active dispersal of the cloud material. Heating and dispersal may compromise future star formation in the warmest regions, and external heating from massive sources may also result in differences between clusters containing OB stars and sparse, low-mass associations. Comparing IC 1396 A to other regions has suggested that the potential for multi-episodic star formation in a cloud may strongly depend on the environment and the effect of the first-formed stars, with OB stars playing a dramatic role in the heating and dispersal of the cloud.

Acknowledgements. We thank Bruno Altieri from the *Herschel* Helpdesk for his valuable help with the data reduction, and Lorenzo Piazzo for making the Unimap code available. We also thank Sofia Sayzhenkova from the computing support at the Departamento de Física Teórica, and both the referee and M. Walmsley, for their useful comments that helped to improve this paper. A.S.A. acknowledges support from the Spanish MICINN/MINECO "Ramón y Cajal" program, grant number RYC-2010-06164, and the action "Proyectos de Investigación fundamental no orientada", grant number AYA2012-35008. C.E. is partly supported by Spanish MICINN/MINECO grant AYA2011-26202. V.R. is supported by the DLR grant number 50 OR 1109 and by the *Bayerischen Gleichstellungsförderung* (BGF). This research made use of Astropy, a community-developed core Python package for Astronomy (Astropy Collaboration, 2013). This research made use of APLpy, an open-source plotting package for Python hosted at http://aplpy.github.com.

References

Abt, H. A. 1986, ApJ, 304, 688
Arzoumanian, D., André, P., Didelon, P., et al. 2011, A&A, 529, L6
Astropy Collaboration 2013, A&A, 558, A33
Barentsen, G., Vink, J. S., Drew, J. E., et al. 2011, MNRAS, 415, 103
Bergin, E. A., Alves, J., Huard, T., & Lada, C. J. 2002, ApJ, 570, L101
Bisbas, T. G., Wünsch, R., Whitworth, A. P., Hubber, D. A., & Walch, S. 2011, ApJ, 736, 142
Caselli, P., Walmsley, C. M., Tafalla, M., Dore, L., & Myers, P. C. 1999, ApJ, 523, L165
Chen, S., & Huang, M. 2010, Res. Astron. Astrophys., 10, 777
Contreras, M. E., Sicilia-Aguilar, A., Muzerolle, J., et al. 2002, AJ, 124, 1585
Elmegreen, B. G. 1998, Origins, 148, 150
Favata, F., Fridlund, C. V. M., Micela, G., Sciortino, S., & Kaas, A. A. 2002, ASP Conf. Ser., 277, 467
Getman, K. V., Feigelson, E. D., Garmire, G., Broos, P., & Wang, J. 2007, ApJ, 654, 316
Getman, K. V., Feigelson, E. D., Luhman, K. L., et al. 2009, ApJ, 699, 1454
Getman, K. V., Feigelson, E. D., Sicilia-Aguilar, A., et al. 2012, MNRAS, 426, 2917
Giardino, G., Favata, F., Silva, B., et al. 2006, A&A, 453, 241
Juvela, M., Montillaud, J., Ysard, N., & Lunttila, T. 2013, A&A, 556, A63
Kessel-Deynet, O., & Burkert, A. 2003, MNRAS, 338, 545
Lippok, N., Launhardt, R., Semenov, D., et al. 2013, A&A, 560, A41
Loren, R. B., Peters, W. L., & Vanden Bout, P. A. 1975, ApJ, 195, 75
Marschall, L. A., & van Altena, W. F. 1987, AJ, 94, 71
Mercer, E. P., Miller, J. M., Calvet, N., et al. 2009, AJ, 138, 7
Miao, J., White, G. J., Thompson, M. A., & Nelson, R. P. 2009, ApJ, 692, 382
Mookerjea, B., Ossenkopf, V., Ricken, O., et al. 2012, A&A, 542, L17
Morales-Calderón, M., Stauffer, J. R., Rebull, L., et al. 2009, ApJ, 702, 1507
Morgan, L. K., Urquhart, J. S., & Thompson, M. A. 2009, MNRAS, 400, 1726
Morgan, L. K., Figura, C. C., Urquhart, J. S., & Thompson, M. A. 2010, MNRAS, 408, 157
Nielbock, M., Launhardt, R., Steinacker, J., et al. 2012, A&A, 547, A11
Ogura, K., Chauhan, N., Pandey, A. K., et al. 2007, PASJ, 59, 199
Ott, S. 2010, Astronomical Data Analysis Software and Systems XIX, ASP Conf. Ser., 434, 139
Patel, N. A., Goldsmith, P. F., Snell, R. L., Hezel, T., & Xie, T. 1995, ApJ , 447, 721
Patel, N. A., Goldsmith, P. F., Heyer, M. H., & Snell, R. L. 1998, ApJ, 507, 241
Peter, D., Feldt, M., Henning, T., & Hormuth, F. 2012, A&A, 538, A74
Piazzo, L. 2013 [arXiv:1301.1246]
Piazzo, L., Ikhenaode, D., Natoli, P., et al. 2012, Artifact removal for GLS map makers by means of post-processing, IEEE Trans. on Image Processing, 21, 3687
Pilbratt, G. L., Riedinger, J. R., Passvogel, T., et al. 2010, A&A, 518, L1
Platais, I., Kozhurina-Platais, V., & van Leeuwen, F. 1998, AJ, 116, 2423
Poglitsch, A., Waelkens, C., Geis, N., et al. 2010, A&A, 518, L2
Pravdo, S. H., Feigelson, E. D., Garmire, G., et al. 2001, Nature, 413, 708
Preibisch, T. 2004, A&A, 428, 569
Preibisch, T., Roccatagliata, V., Gaczkowski, B., & Ratzka, T. 2012, A&A, 541, A132
Prisinzano, L., Micela, G., Flaccomio, E., et al. 2008, ApJ, 677, 401
Reach, W., Rho, J., Young, E., et al. 2004, ApJS, 154, 385
Roccatagliata, V., Preibisch, T., Ratzka, T., & Gaczkowski, B. 2013, A&A, 554, A6
Sicilia-Aguilar, A., Hartmann, L., Briceño, C., Muzerolle, J., & Calvet, N. 2004, AJ, 128, 805
Sicilia-Aguilar, A., Hartmann, L., Hernández, J., Briceño, C., & Calvet, N. 2005, AJ, 130, 188
Sicilia-Aguilar, A., Hartmann, L., Calvet, N., et al. 2006a, ApJ, 638, 897
Sicilia-Aguilar, A., Hartmann, L., Fürész, G., et al. 2006b, AJ, 132, 2135
Sicilia-Aguilar, A., Henning, Th., Juhász, A., et al. 2008, ApJ, 687, 1145
Sicilia-Aguilar, A., Henning, T., Dullemond, C. P., et al. 2011, ApJ, 742, 39
Sicilia-Aguilar, A., Henning, T., Linz, H., et al. 2013a, A&A, 551, A34
Sicilia-Aguilar, A., Kim, J. S., Sobolev, A., et al. 2013b, A&A, 559, A29
Siess, L., Dufour, E., & Forestini, M. 2000, A&A, 358, 593
Simonson, S. C., & van Someren Greve, H. V. 1976, A&A, 49, 343
Sugitani, K., & Ogura, K. 1994, ApJS, 92, 163
Sugitani, K., Fukui, Y., & Ogura, K. 1991, ApJS, 77, 59
Ward-Thompson, D., André, P., & Kirk, J. M. 2002, MNRAS, 329, 257
Weikard, H., Wouterloot, J. G. A., Castets, A., Winnewisser, G., & Sugitani, K. 1996, A&A, 309, 581